Performance and Flowfield Measurements on a 10-inch Ducted Rotor VTOL UAV

Preston Martin* and Chee Tung†
Army / NASA Rotorcraft Division
Aeroflightdynamics Directorate, AMRDEC
US Army Research, Development, and Engineering Command
Ames Research Center, Moffett Field, CA 94035

A ducted fan VTOL UAV with a 10-inch diameter rotor was tested in the US Army 7-by 10-Foot Wind Tunnel. The test conditions covered a range of angle of attack from 0 to 110 degrees to the freestream. The tunnel velocity was varied from 0 (simulating a hover condition) to 120 ft/sec in propeller mode. A six-component internal balance measured the aerodynamic loads for a range of model configurations, including the isolated rotor, the isolated duct, and the full configuration of the duct and rotor. For some conditions, hotwire velocity surveys were conducted along the inner and outer surface of the duct and across the downstream wake. In addition, fluorescent oil flow visualization allowed the flow separation patterns inside and outside of the duct to be mapped for a few test conditions. Two different duct shapes were tested to determine the performance effects of leading edge radius. For each duct, a range of rotor tip gap from 1%R to 4.5%R was tested to determine the performance penalty in hover and axial flight. Measured results are presented in terms of hover performance, hover performance in a crosswind, and high angle of attack performance in propeller mode. In each case, the effects of both tip gap and duct leading edge radius are illustrated using measurements. Some of the hover performance issues were also studied using a simple analytical method, and the results agreed with the measurements.

Nomenclature

A	Rotor disk area, πR^2
c	Duct airfoil chord, *in*
C_l	Lift coefficient
C_m	Pitching moment coeff. about $c/4$, + nose up
C_p	Pressure coefficient, $= (P_o - P_s)/q$
C_P	Rotor power coefficient
C_T	Thrust coefficient
D	Inner-diameter of duct, *in*
FM	Total system figure of merit, $C_T^{3/2}/(\sqrt{2}C_P)$
P_o	Local static pressure, lbs/ft^3
P_s	Freestream static pressure, lbs/ft^3
P_i	Total pressure, lbs/ft^3
q	Freestream dynamic pressure, lbs/ft^3
Re	Reynolds number based on chord length
r_{LE}	Leading edge radius of duct airfoil, *in*
r_c	Rotor blade root cut-out, *in*
R	Rotor radius, *in*
V_o	Freestream velocity, ft/sec, kts
α	Angle of attack, *deg*
Δr_t	Tip gap between rotor and duct, *in*
ρ	Density, $slug/ft^3$
μ	Advance ratio

Introduction

Recent military operations in urban environments have stimulated research into small-scale ducted fan vertical take-off and landing (VTOL) uninhabited aerial vehicles (UAVs). The current concept of an "organic" air vehicle (OAV) relates to a small-scale, portable UAV operated by a single soldier in the field. Development efforts have made considerable progress in fielding such a system, but some of the fundamental aerodynamic issues are only starting to be identified through operational problems and performance limitations. Research on ducted propellers has progressed from some of the first systematic testing by Kruger, Ref. 1, to recent application of the fenestron to helicopter tail rotors (Ref. 2). Several tests have been conducted by NASA at Ames Research Center including advanced shrouded propellers (Refs. 3 and 4) and more recently, a ducted fan for a personal transport rotorcraft (Ref. 5).

For this new class of small UAVs, and for micro UAVs in general, the duct diameter is on the order of a few inches. The result is very low Reynolds number flows inside the duct and incident to the rotor blades. The focus on hover efficiency of ducted rotors at low Reynolds number is a new and interesting area of research. There are numerous efforts in government, industry, and academic communities aimed at the analysis and design for this class of vehicle. These tools and methods require some very simple test cases for validation and development.

The objective of this experimental study was to obtain a baseline test case using a simple geometry for CFD validation and design tool development. In addition to performance data, the flowfield measurements and visualization both provided insight into the primary flow physics associated with this class of UAV.

Experimental Apparatus and Procedure

The experimental setup included a 10-inch diameter powered ducted fan wind tunnel model mounted in a 7 by 10 foot test section (Fig. 1a). The wind tunnel blockage was less than 2% including the support hardware. Force and moment data were acquired with a sting mounted 0.75-inch, 6-component internal balance as shown in Fig. 1 b. The metric side of

*Research Scientist
†Deputy Branch Chief - Aeromechanics

Report Documentation Page

Form Approved
OMB No. 0704-0188

1. REPORT DATE	2. REPORT TYPE	3. DATES COVERED
JUN 2004		**00-00-2004 to 00-00-2004**

4. TITLE AND SUBTITLE	5a. CONTRACT NUMBER
Performance and Flowfield Measurements on a 10-inch Ducted Rotor VTOL UAV	5b. GRANT NUMBER
	5c. PROGRAM ELEMENT NUMBER
6. AUTHOR(S)	5d. PROJECT NUMBER
	5e. TASK NUMBER
	5f. WORK UNIT NUMBER
7. PERFORMING ORGANIZATION NAME(S) AND ADDRESS(ES) **US Army Research, Development, and Engineering Command,Army/NASA Rotorcraft Division,Aeroflightdynamics Directorate, AMRDEC,Moffett Field,CA,94035**	8. PERFORMING ORGANIZATION REPORT NUMBER
9. SPONSORING/MONITORING AGENCY NAME(S) AND ADDRESS(ES)	10. SPONSOR/MONITOR'S ACRONYM(S)
	11. SPONSOR/MONITOR'S REPORT NUMBER(S)

12. DISTRIBUTION/AVAILABILITY STATEMENT
Approved for public release; distribution unlimited

13. SUPPLEMENTARY NOTES
Proceedings of the 60th Annual Forum of the American Helicopter Society, Baltimore, MD, June 7-10, 2004

14. ABSTRACT

15. SUBJECT TERMS

16. SECURITY CLASSIFICATION OF:			17. LIMITATION OF ABSTRACT	18. NUMBER OF PAGES	19a. NAME OF RESPONSIBLE PERSON
a. REPORT **unclassified**	b. ABSTRACT **unclassified**	c. THIS PAGE **unclassified**	**Same as Report (SAR)**	**20**	

the balance measured the forces and moments on the model, including the motor and gearbox. Hotwire velocity surveys were conducted using a three-axis traverse and a single wire probe shown in Fig. 1 c. Surface flow visualization was acquired using fluorescent oil illuminated by ultra-violet lights, see Fig. 1 d.

US Army 7-by 10-Foot Wind Tunnel

All testing was completed in the US Army 7-by 10-Foot Wind Tunnel at NASA Ames Research Center, see Figs. 1 (a) and 2. The tunnel has a 14:1 contraction ratio and is powered by a 30-ft diameter fan. The turbulence levels in the freestream are less than 0.5% in all three components. While the tunnel has air exchange capability, the louvers were closed during these tests to insure the highest flow quality at low tunnel speeds. The test section dynamic pressure was measured using a pair of static pressure rings located at the entrance and exit to the tunnel contraction section. In addition, a pitot-static probe was mounted at the entrance to the test section for improved accuracy at low tunnel speed and to determine test section flow induced by the rotor operating in hover mode.

Ducted Fan VTOL UAV Model

The objective of the experiment was to provide a simple baseline test case for CFD validation and design tool development. The wind tunnel model was designed and manufactured by Techsburg, Inc. based on past experience in testing UAVs. The baseline duct shape was representative of early designs for a small ducted fan UAV and was characterized by a large leading edge radius $r_{LE}/c = 0.05$ and a thickness-to-chord ratio of $t/c = 0.20$, where the chord, c, is referenced to the duct airfoil cross section, $c = 5.77in$. The second duct shape tested was similar, but was designed with a smaller leading edge radius $r_{LE}/c = 0.03$ and a thickness-to-chord ratio of $t/c = 0.19$.

A typical ducted fan UAV configuration includes stators, control vanes, and sensor packages; however, this wind tunnel model was simplified and did not include any of these items. The reason for the simplification was to provide a very basic test case for CFD analysis. Two small NACA 0012 support struts were the only structure within the rotor slipstream. The outer diameter of the motor housing was designed to be less than the rotor root cutout of $r_c/R = 0.33$ in order to avoid excessive hub blockage.

The configuration of the model is shown in Fig. 3. The model included a 10-inch inner diameter duct, and a 2-bladed rotor with a radius that ranged from 4.95 in to 4.80 in for studying the effects of tip gap. The spinner shown in Fig. 3 was not used, and so the hub geometry was that shown in Fig. 1 c and d. Both ducts tested were constant internal diameter along the length, except for a very small region near the trailing edge.

Test Conditions

The test matrix covered a range of tunnel speeds from no flow (simulating hover out of ground effect) to 120 ft/sec simulating a high rate of advance in propeller mode. At each speed, the angle of attack (Fig. 4) was varied using a floor mounted turn table (i.e., the model was on its side). The turn table provided angles of attack from 0 degrees (propeller mode, axial climb) to 110 degrees (hover with cross flow). For some cases, the angle of attack was varied in increments of 1 to 2 degrees to map out the stall behavior of the isolated duct and the duct/rotor configuration. For the hover configuration, the rotor RPM was varied from 2000 to 9500.

The zero angle of attack speed sweeps and no flow RPM sweeps were repeated for different rotors with a range of tip gap from $\Delta r_t/R = 0.01$ to 0.045. The tip gap is defined as the radial distance from the rotor tip to the inner wall of the duct as shown by Fig. 7.

A six-component internal balance measured the aerodynamic loads for a range of model configurations, including the isolated rotor, the isolated duct, and the full configuration of the duct and rotor. For some conditions, hotwire velocity surveys were conducted along the inner and outer surface of the duct and across the downstream wake. In addition, fluorescent oil flow visualization allowed the flow separation patterns inside and outside of the duct to be mapped for a few test conditions.

Results and Discussion

A typical mission profile for a small ducted fan rotorcraft would begin with a take-off vertical followed by a transition to propeller mode. After arriving on station, the vehicle would then transition to hover and loiter while acquiring sensor data. The most important design specifications for a portable VTOL UAV are hover efficiency, hover control in adverse winds, and stall performance in propeller mode. Based on these priorities, the following measured results are presented in terms of hover performance, hover performance in a crosswind, and high angle of attack performance in propeller mode. In each case, the effects of both tip gap and duct leading edge radius are illustrated.

Hover Performance

The hover performance data is divided into the isolated rotor results and the ducted rotor results. The load sharing between the duct and rotor was roughly approximated by the difference between the isolated rotor performance compared to that of the ducted rotor. Owing to the small scale of these tests, the balance measured the total thrust, and so the individual contributions of the components cannot be determined exactly. In this case, a more accurate approach would have required testing a ducted rotor with a modified twist distribution to account for the induced flow generated by the duct circulation.

Isolated Rotor

For the hover test condition, the isolated rotor (duct removed) was first operated over a range of RPM. A series of rotors was tested with slightly different values of the blade radius to investigate the effect of the gap between the rotor tip and duct. In order to measure each case against the ideal case of zero tip gap, the tip speed was taken as the actual value based on each of the blade radii; however, the duct internal radius was always used when computing the reference area. This procedure was also used for the unducted cases, and so the slight change in tip twist with the reduction of blade radius was offset. Using this method with the duct removed, all of the rotors collapse to a single thrust coefficient that is only slightly sensitive to RPM (i.e., Reynolds number), see Fig 5.

Ducted Rotor

The ducted rotor thrust coefficient is compared to the isolated rotor in Fig. 6 over a range of RPM. The results are shown for 3 values of tip gap defined in Fig. 7, and only one isolated rotor case is used for clarity. As shown by Fig. 6, the load sharing between the duct and rotor (at high RPM) is a strong function of tip gap. For the smallest tip gap of $\Delta r_t/R = 0.01$, the duct thrust developed to approximately 38% of the isolated rotor thrust at high RPM.

A very interesting result occured as the RPM was reduced, and the Reynolds number of the flow through the duct decreased in Fig. 6. This phenomenon is either due to the loss of the suction peak on the duct lip from laminar separation, or more likely due to the viscous losses inside the duct. The internal flow losses tend to counteract the duct thrust, and below a certain RPM the duct produces a net download (compared to the isolated rotor). This result is very important for the design and analysis of micro UAVs that would be even smaller than the vehicle tested in this study.

Another key result of this study was measuring the sensitivity of hover efficiency to increasing tip gap as shown in Fig. 8. In order to facilitate an equal comparison of the isolated rotor to the ducted rotor, the figure of merit for the total system was defined as

$$FM = \frac{C_T^{3/2}}{\sqrt{2}C_P} \tag{1}$$

where the thrust coefficient includes the duct forces. Note that the ideal power for the ducted rotor was assumed to be the same as for the isolated rotor in order to compare the figure of merit. As the tip gap was increased, the ducted rotor figure of merit approached the isolated rotor figure of merit ($FM = 0.44$) in Fig. 8.

Another method of defining the figure of merit for the ducted rotor would have been to use a zero wake contraction assumption for the induced power estimate, however this method was not used. The difference in the methods was not important for measuring the change in figure of merit as a function of tip gap. The system power was measured using the electrical power supplied to the motor, and so the losses across the gearbox and motor controller are included in both the ducted and un-ducted cases.

The tip gap effect was studied in more detail using a potential flow analytical method similar to Ref. 6. The rotor was modeled with a vortex column, and the duct was modeled as a series of vortex rings around the airfoil surface, as described in Ref 7. Example results are shown in Fig. 9, where the velocity field is shown for 5% and 1% tip gap. The duct static pressure distribution is also shown to the right of Fig. 9 for increasing tip gap. As the tip gap is increased, the suction pressure near the leading edge rapidly collapses in Fig. 9, and so the duct lift decreases as shown by the measured data in Fig. 6.

The same results were repeated for a different duct shape. The duct thrust is also reduced by a decrease in the duct leading edge radius (see Fig. 10). At low Reynolds numbers the effect of duct leading edge radius is more pronounced than higher Reynolds number data from Ref. 1 compared in Fig. 11. The same result was observed in the potential flow analytical results shown to the left of Fig. 11.

Hover performance in a cross-wind

Measurements of hover performance in a cross-wind were achieved by turning the duct $\alpha = 90^\circ$ to the wind tunnel freestream. The model was positioned close to the center of the wind tunnel yaw turn-table, and so the model remained in the same tunnel location during the angle sweeps. The pitching moment was resolved to the duct quarter-chord and defined by the hover tip speed instead of the freestream dynamic pressure. An example variation of pitching moment with crosswind speed is shown in Fig. 12. A positive pitching moment is defined as tilting the upwind side of the duct upwards. The positive increase in pitching moment with speed creates a control instability that is a severe problem for these types of vehicles.

The angle was also varied $+10^\circ$ to -30° from hover to simulate climb and descent in a 24-knot crosswind as shown in Fig. 13. In this figure, the results are plotted for two different duct lip shapes. While the small leading edge radius showed a decrease in hover performance, it also favorably decreased the magnitude of the speed instability. This was accomplished by the flow separating over the sharp leading edge; and therefore, the asymmetric suction pressure forming around the duct lip was less severe than the more blunt leading edge. The blunt leading edge promoted the formation of a strong asymmetric suction pressure around the duct lip. This caused a pitching moment in the direction of tilting the rotor away from the oncoming flow. A reduction in this pitching moment results in a more stable platform for station keeping missions in a cross-wind.

High α Performance

The high angle of attack performance was studied for the duct alone (as in Ref. 8), and for the ducted rotor. As shown by Fig. 14, the maximum lift coefficient and stall angle vary considerably for the isolated duct compared to the powered duct. While the un-powered duct stalled near 15 degrees (similar to an airfoil), the powered duct did not stall until 40 degrees angle of attack. The stall delay and the vertical component of the thrust vector allowed the powered duct to achieve five-times the maximum lift coefficient of the duct alone. The flow physics that contribute to the stall were investigated using oil flow visualization and hotwire boundary layer measurements, see Fig. 15, for the combined rotor and duct configuration. The outer surface of the duct is characterized by a laminar separation bubble followed by a significant amount of turbulent separation even at zero angle of attack. These features are important for understanding CFD validation results and for the development of design tools.

The minor effect of tip gap on the stall performance is shown in Fig. 16. In this figure, the data for the smallest tip gap ends before reaching $\alpha = 30^\circ$. At the data point after the last one shown in Fig. 16 for $\Delta r_t/R = 0.01$, the severe vibrations caused by flow separation on the upper, outer surface resulted in contact between the rotor tip and the inside of the duct. For the case of $\Delta r_t/R = 0.02$, the model experienced severe buffetting at angles of attack near $\alpha = 40^\circ$ where the vehicle stalled. The unsteady loads in this flow regime approached the balance dynamic capacity, and so no data was acquired beyond these angles at 35 knots. It is interesting to note that this condition is near the cruise trim state for some

current operational vehicles.

The effect of duct shape on stall is shown in Figs. 17 and 18. Positive pitching moment is defined as nose up. The small leading edge radius duct was designed to improve the high angle of attack performance, and it appears (by the decreased magnitude of the pitching moment) that some of the flow separation on the outer side of the duct was alleviated. In the baseline case, the flow separation on the outer side of the duct trailing edge causes a high pressure region responsible for the positive (nose up) pitching moments.

Hotwire Flow Survey

In addition to performance data, hotwire velocity surveys were conducted inside and outside of the duct, and in the wake. Example velocity profiles near the duct exit are shown in Fig. 19. An interesting result was that the time averaged boundary layer thickness measured inside the duct was much greater than the outer surface as shown by Fig. 20. In this figure, the line of peak turbulent fluctuation is shown in red, and the wake boundary is shown in blue. On the outer side of the wake, the peak fluctuation occurs near the minimum velocity line; however, on the inside of the wake the peak fluctuation appears away from the middle of the shear layer. Further analysis of the hotwire signals showed a periodic frequency indicating the presence of tip vortices along this line of peak fluctuation (Fig. 20 shows a slight wake contraction). The flow physics in this region and along the inside wall of the duct appears to be governed by the interaction of the rotor, tip vortices, and the duct boundary layer. Surface flow visualization shown in Fig. 21 indicates that the flow separates immediately upon passing the rotor tip path plane. There was zero skin friction measured by the oil flow patterns downstream of the tip path plane.

Conclusions

1. A 10-inch ducted rotor was tested over a range of flow conditions for two different duct shapes and a range of rotor tip gaps.

2. At low RPM (i.e., low Reynolds number), it appeared that the viscous losses of the duct internal flow counteracted the duct thrust. Below a certain RPM, the net force contribution from the duct was a download when compared to the isolated rotor. This is an important result for the design of micro UAVs.

3. Measurements and analytical results showed that increasing the rotor tip gap decreased the duct thrust dramatically and therefore decreased the total figure of merit of the vehicle.

4. A decrease in duct leading edge radius caused a decrease in the ratio of duct thrust to isolated rotor thrust in both measurements and simple analytical results, but improved the stability for hover in a crosswind.

5. The stall performance of the isolated duct was very different from that of the powered duct. The un-powered duct stalled near 15 degrees, and the powered duct did not stall until 40 degrees angle of attack. The powered duct achieved five-times the maximum lift coefficient of the duct alone.

6. The small leading edge radius duct shape improved the pitching moment during stall, but the stall angle and maximum lift were not changed and appear to be governed by the rotor performance.

7. A complex interaction between the rotor, tip vortex, and duct boundary layer appeared in both the hotwire measurements and surface flow visualization. The flow along the inner wall of the duct appeared to separate after passing through the rotor tip path plane.

Acknowledgments

The support and cooperation of Dr. William Warmbrodt, Joel Gunter, Bruce Gesek, Steve Chan, Brian Chan, Jon Lautenschlager, Farid Haddad, and Bruce Storms were greatly appreciated. The authors would also like to thank Troy Jones and Dr. Jon Fleming of Techsburg, Inc. for the design and fabrication of the wind tunnel model. The authors give a special thanks to Brent Wellman for the design of the balance/sting interface. Finally, the invaluable assistance of Sarah Mertens and Josh Johnson of the NASA Undergraduate Student Research Program was greatly appreciated.

References

[1]Kruger, W., "On Wind Tunnel Tests and Computations Concerning the Problem of Shrouded Propellers," NACA TM 1202, 1949.

[2]Vialle, M., and Arnaud, G., "A New Generation of Fenestron Fan-in-Fin Tail Rotors on EC 135," 19th European Rotorcraft Forum, Cernobbio (Como), Italy, Sept., 1993.

[3]Mort, K. W., and Gamse, B., "A Wind-Tunnel Investigation of a 7-Foot-Diameter Ducted Propeller," NASA TN D-4142, 1967.

[4]Mort, K. W., "Performance Characteristics of a 4-Foot-Diameter Ducted Fan at Zero Angle of Attack for Several Fan Blade Angles," NASA TN D-3122, 1965.

[5]Abrego, A. I., and Bulaga, R. W., "Performance Study of a Ducted Fan System," American Helicopter Society, Aerodynamics, Acoustics, and Test and Evaluation Technical Specialist Meeting, San Francisco, CA, Jan., 2002.

[6]Mendenhall, M. R., and Spangler, S. B., "A Computer Program for the Prediction of Ducted Fan Performance," NASA CR-1495, 1970.

[7]Kuchemann, D., and Weber, J., *Aerodynamics of Propulsion*, McGraw-Hill, New York, 1953.

[8]Fletcher, H. S., "Experimental Investigation of Lift, Drag, and Pitching Moment of Five Annular Airfoils," NACA TN 4117, 1957.

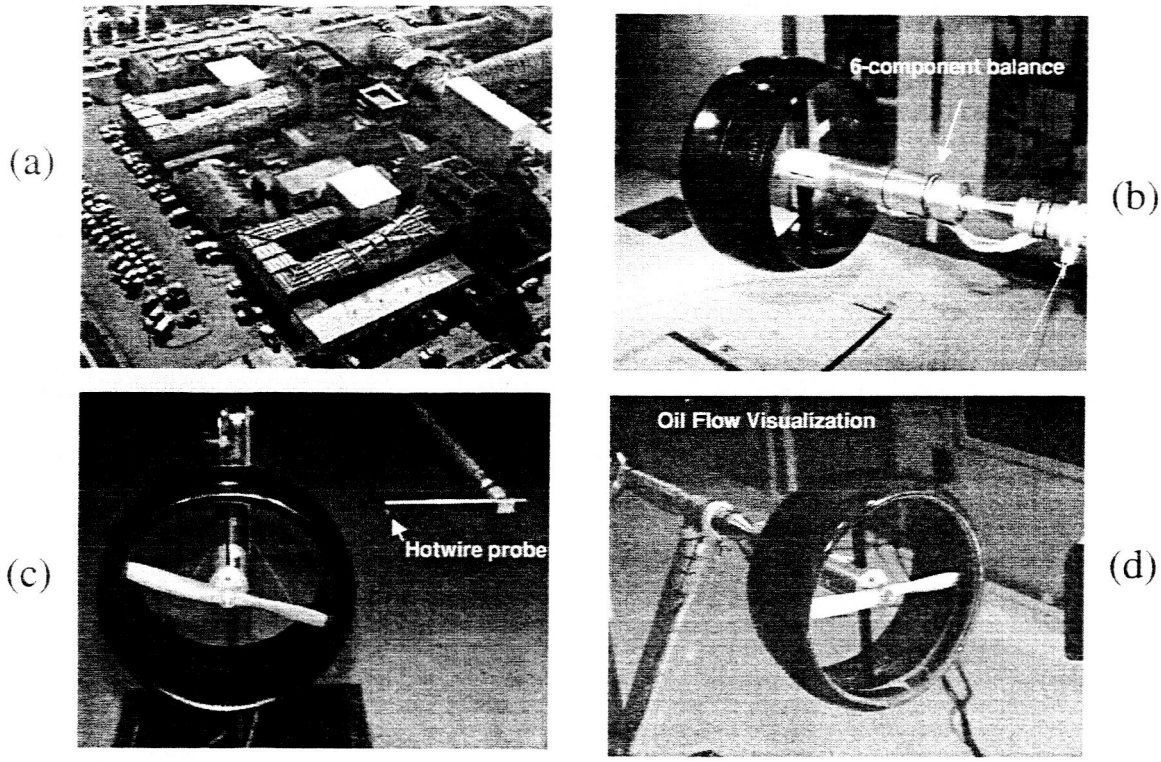

Fig. 1 Test configuration: (a) US Army 7-by 10-Foot Wind Tunnel (b) Sting mounted six-component balance (c) Hotwire probe configured for wake survey (d) Fluorescent oil flow visualization.

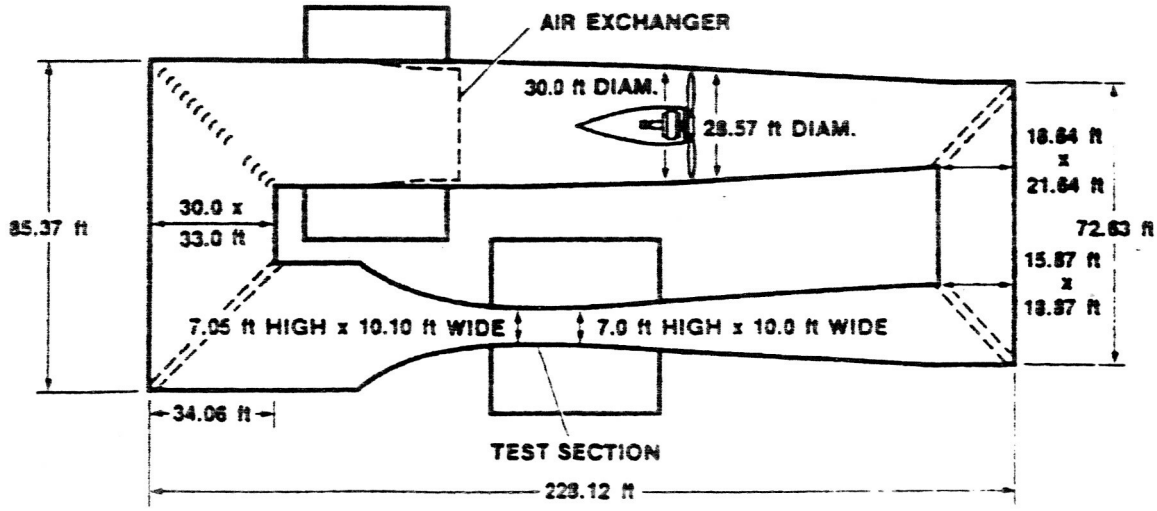

Fig. 2 US Army 7-by 10-Foot Wind Tunnel circuit diagram.

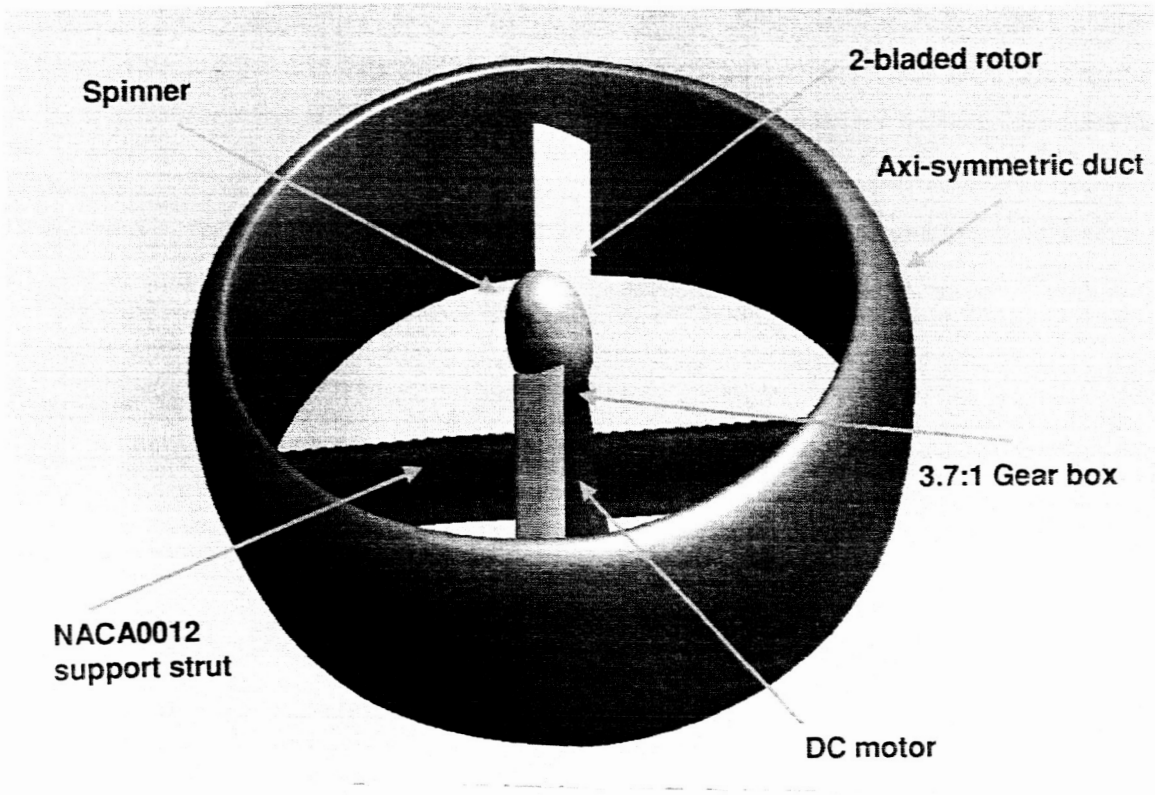

Fig. 3 Schematic of 10 in. ducted fan VTOL UAV wind tunnel model.

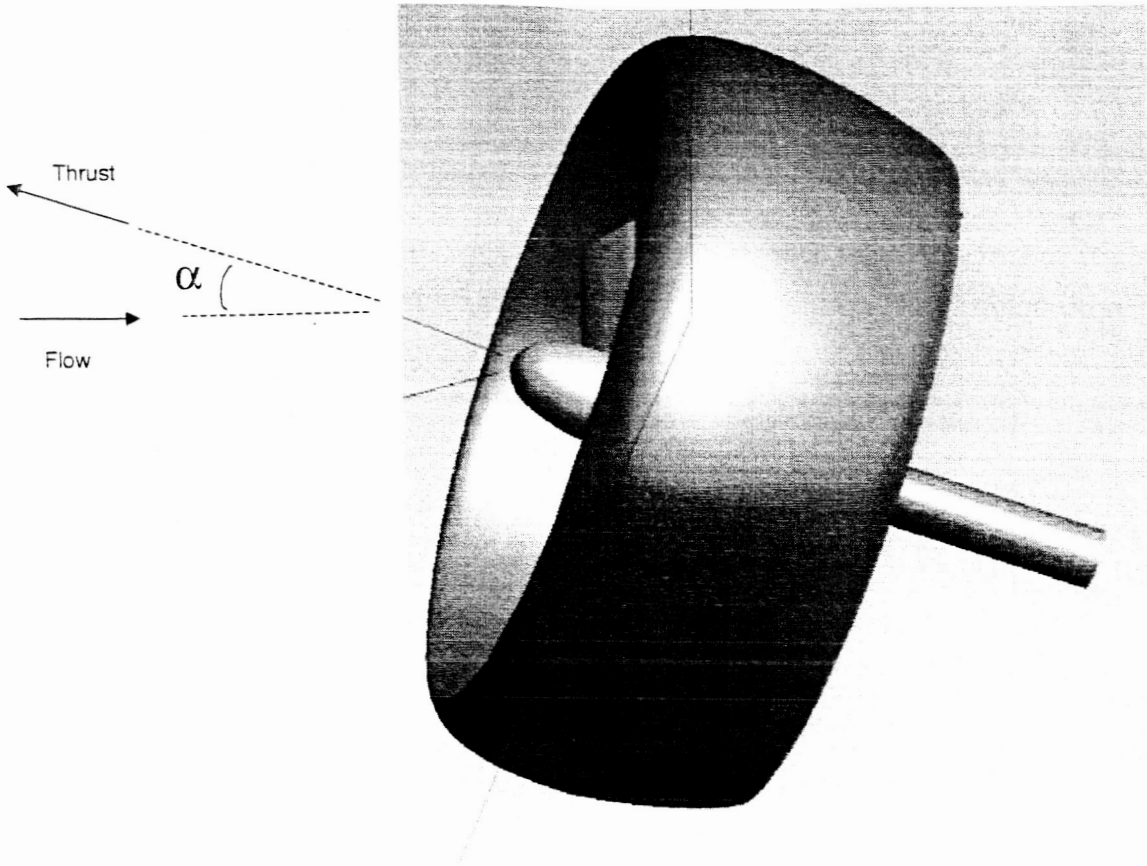

Fig. 4 Definition of angle of attack α in forward flight.

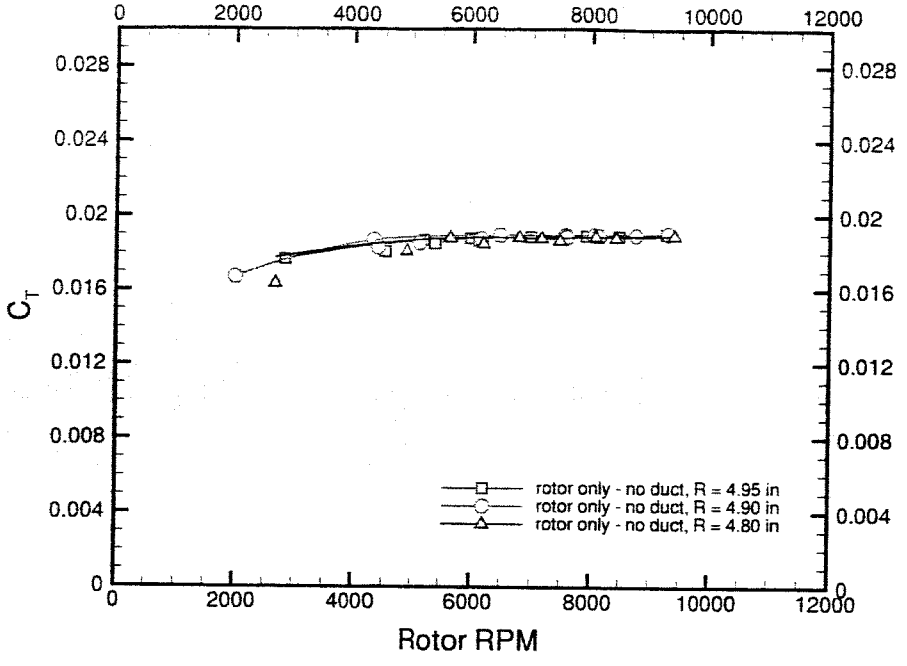

Fig. 5 Baseline hover performance for the isolated rotors over a range of RPM.

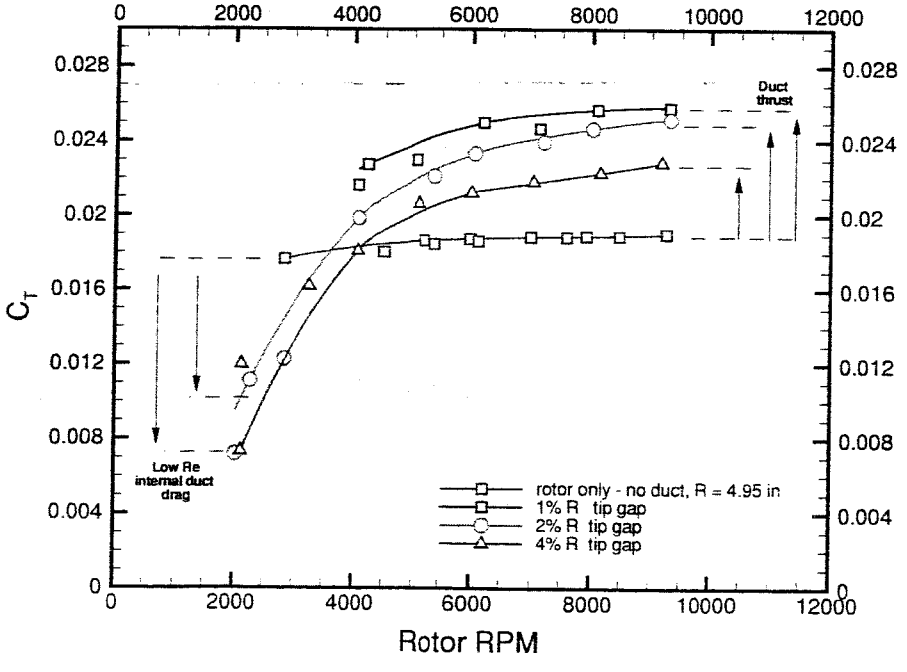

Fig. 6 Thrust variation with RPM and tip gap for large leading edge radius duct, $r_{LE}/c = 0.05$.

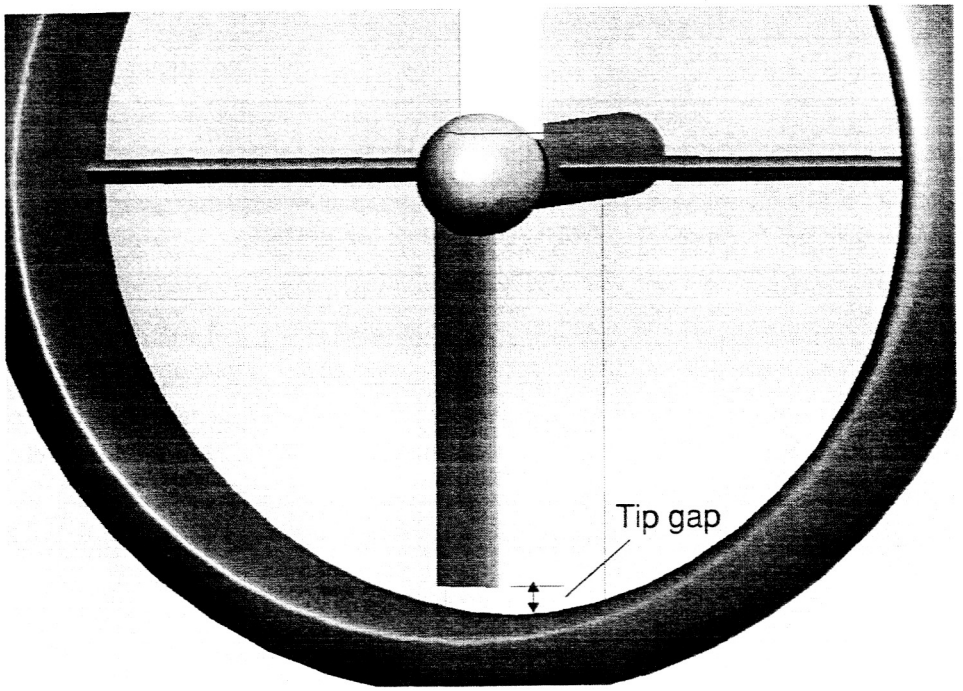

Fig. 7 Definition of tip gap Δr_t.

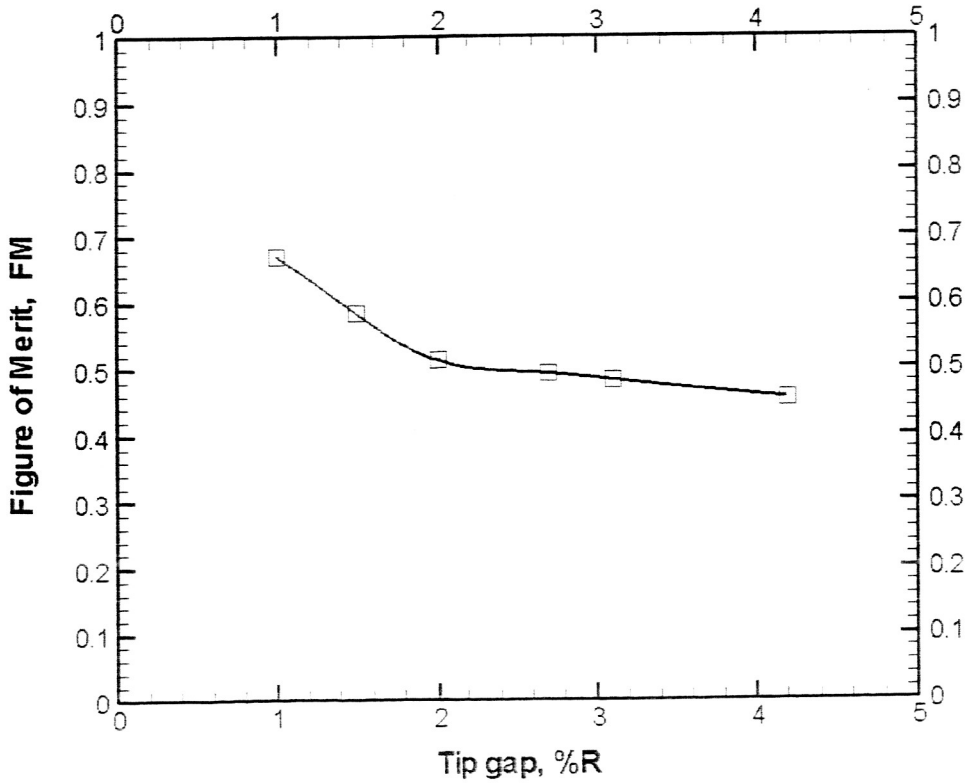

Fig. 8 Effect of tip gap on figure of merit in hover, $r_{LE}/c = 0.05$, 9000 RPM. Isolated rotor figure of merit, $FM = 0.44$.

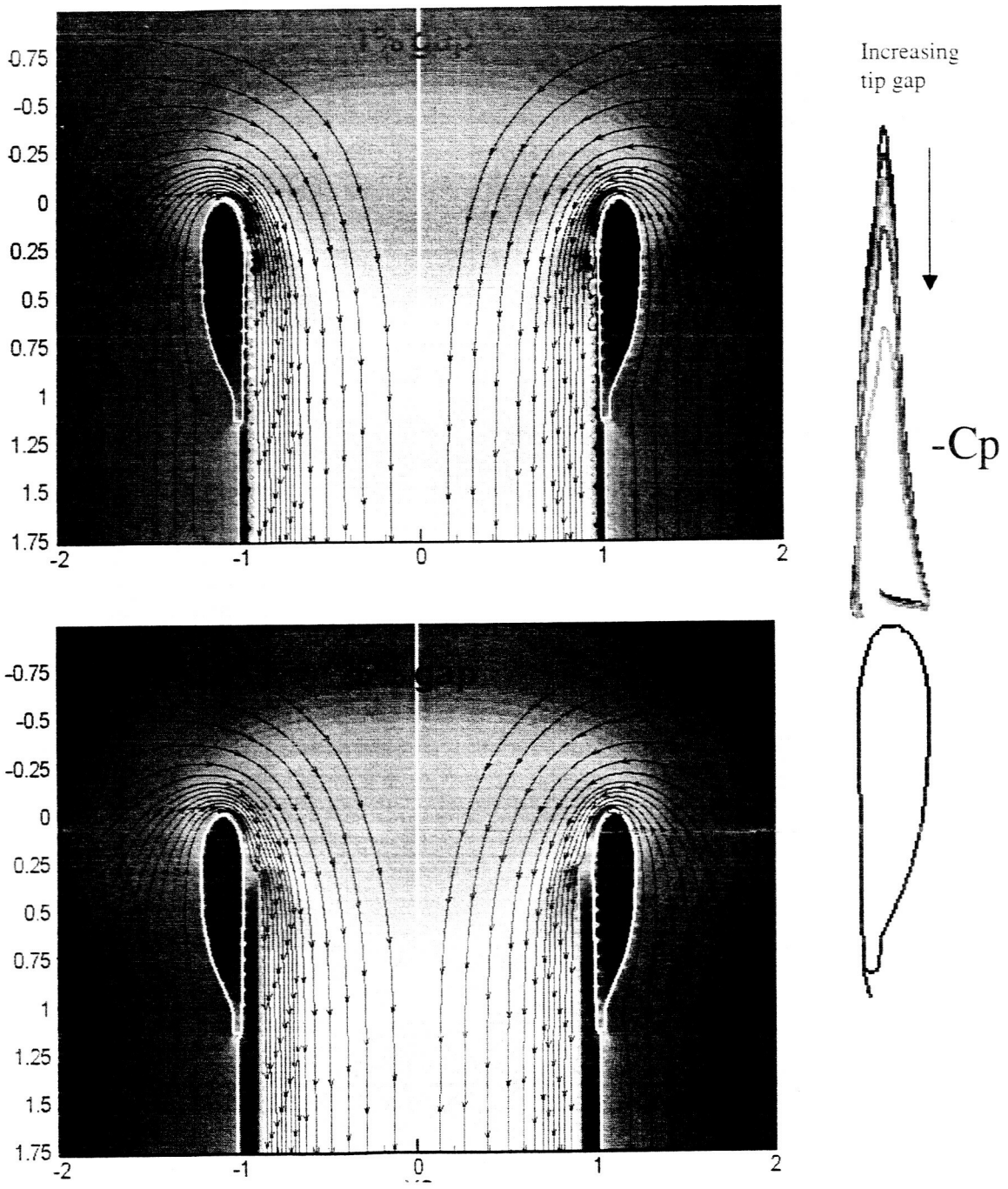

Fig. 9 Analytical results for the effect of tip gap on the duct static pressure distribution.

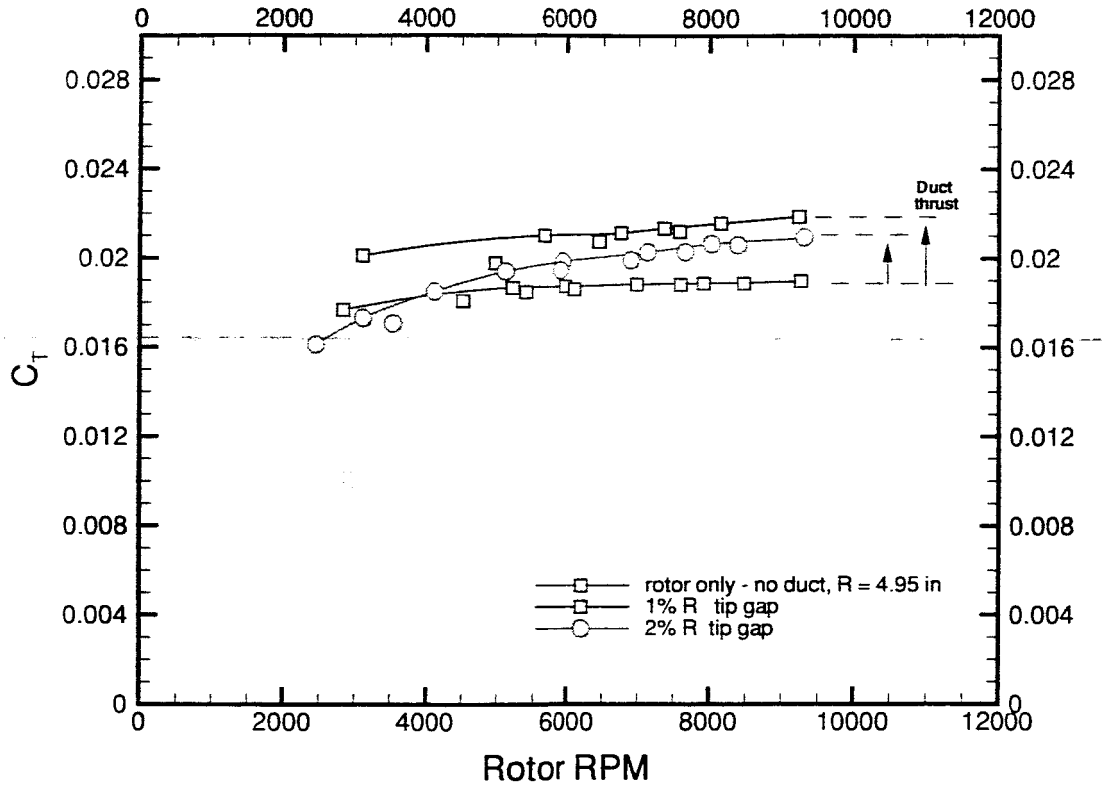

Fig. 10 Thrust variation with RPM and tip gap for small leading edge radius duct, $r_{LE}/c = 0.03$.

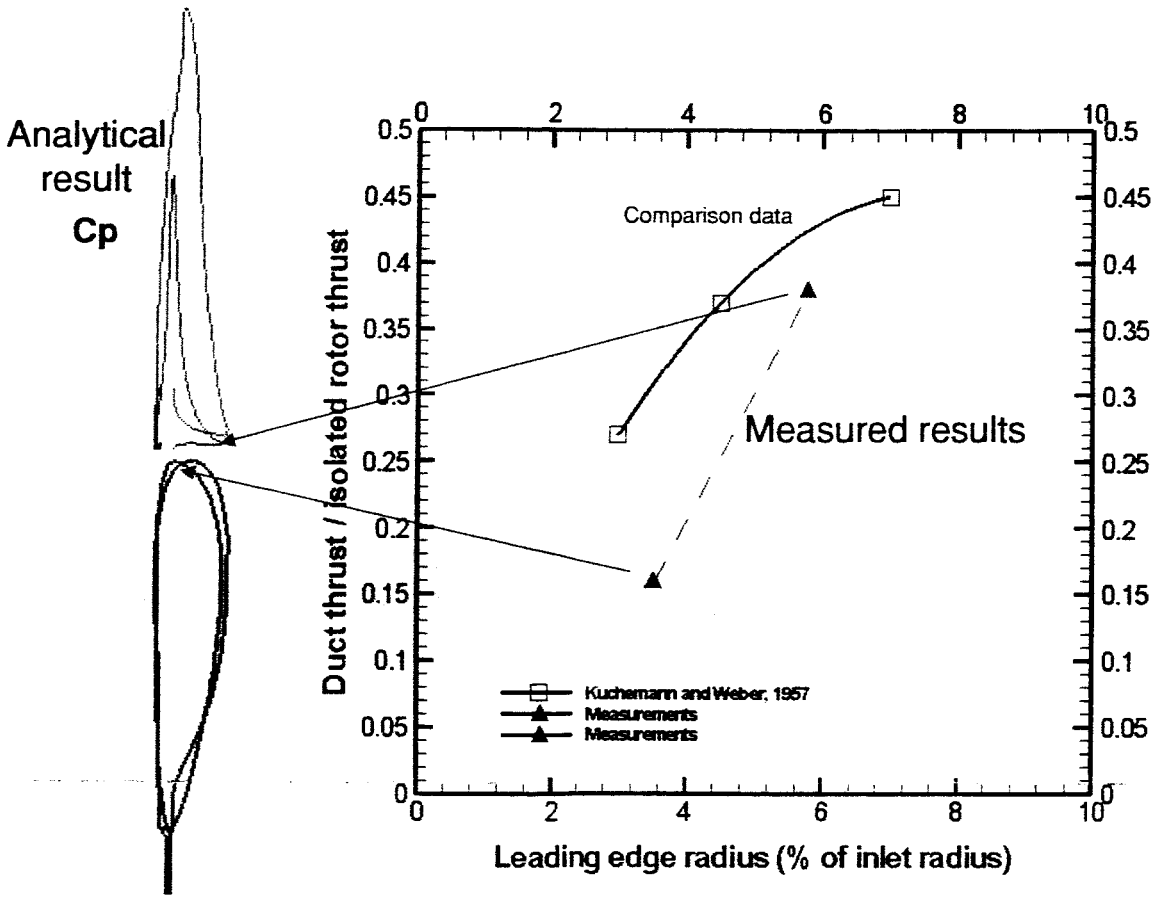

Fig. 11 Effect of duct leading edge radius on load sharing, 9000 RPM.

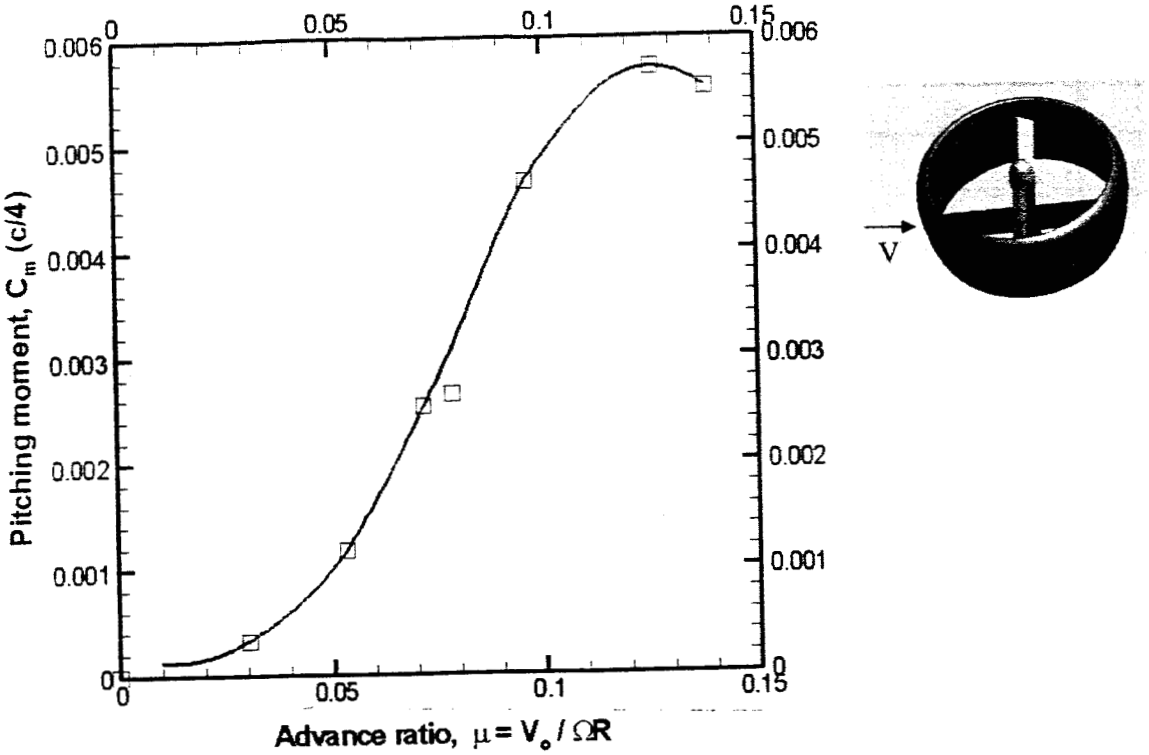

Fig. 12 Development of pitching moment instability in hover with increasing crosswind velocity component, $r_{LE}/c = 0.05, \Delta r_t/R = 0.02$, 9000 *RPM*.

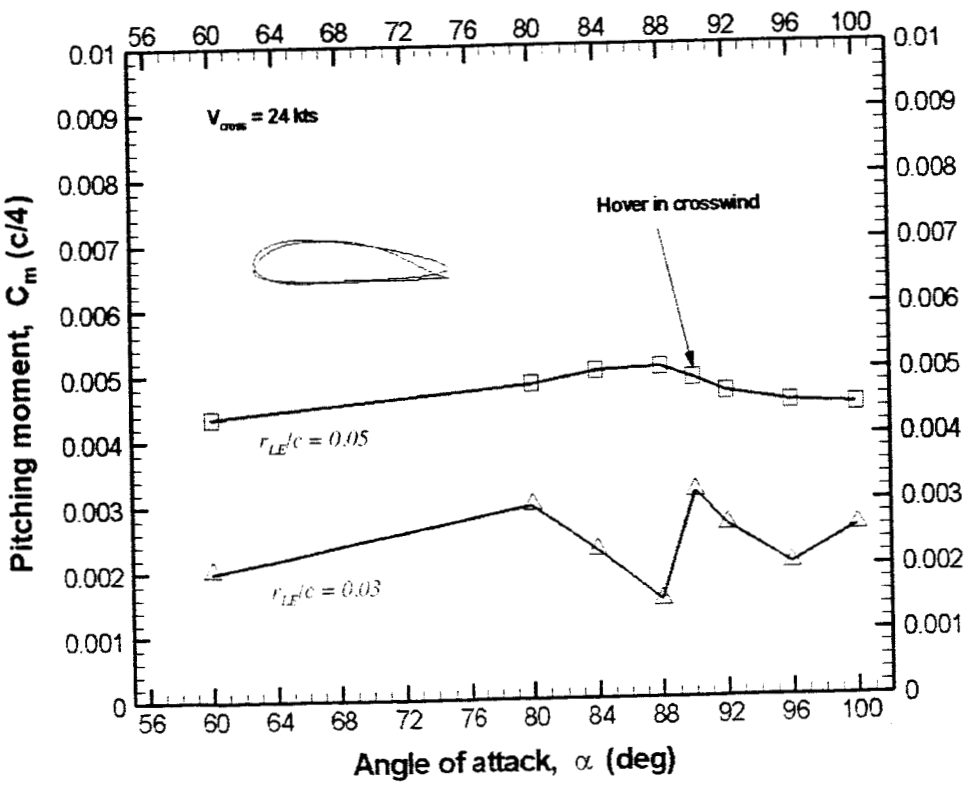

Fig. 13 Alleviation of pitching moment instability in hover with decrease in duct leading edge radius, $\Delta r_t/R = 0.02, V_o = 24$ *kts*, 9000 *RPM*.

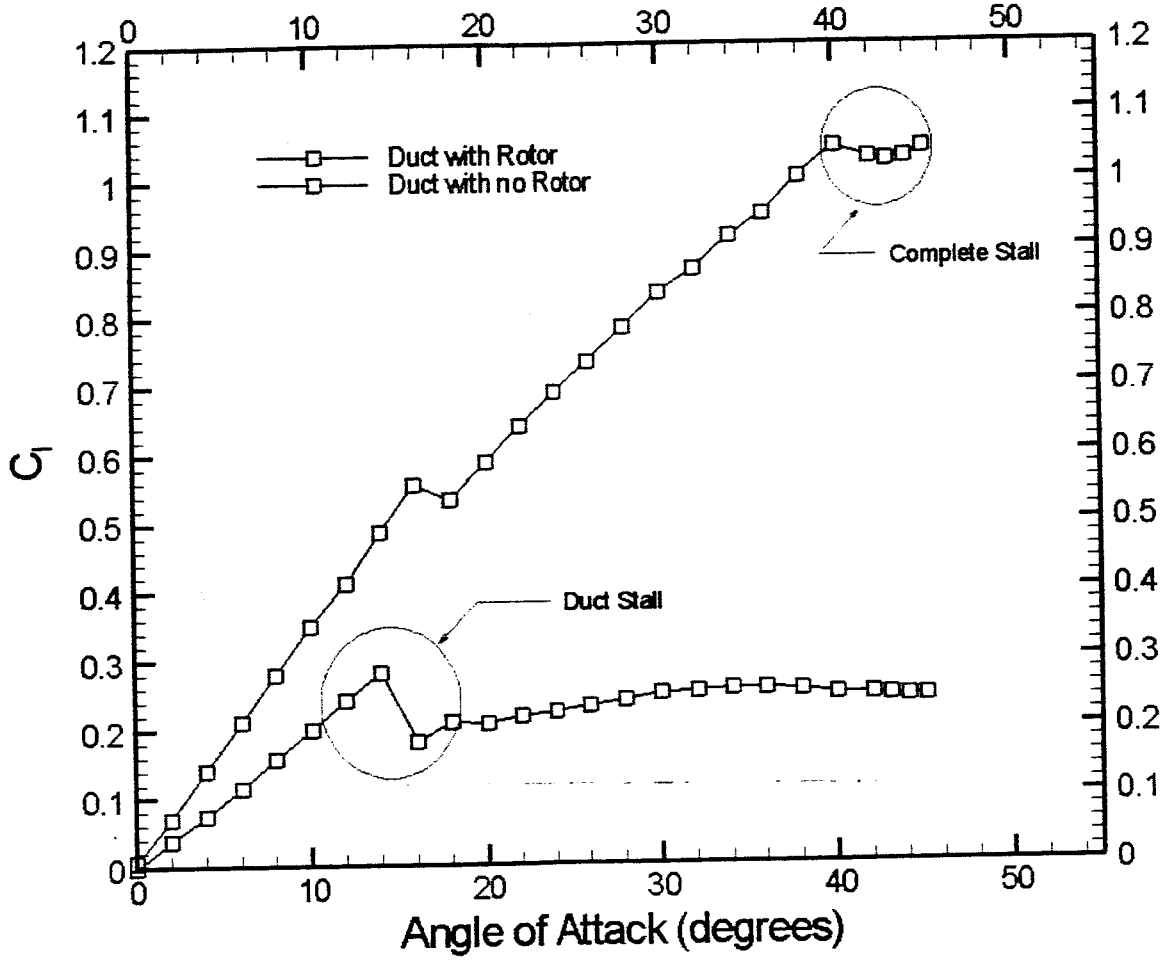

Fig. 14 Comparison of stall performance of isolated duct and rotor/duct combination. $r_{LE}/c = 0.05, \Delta r_t/R = 0.02, V_o = 35$ *kts*, 9000 *RPM*.

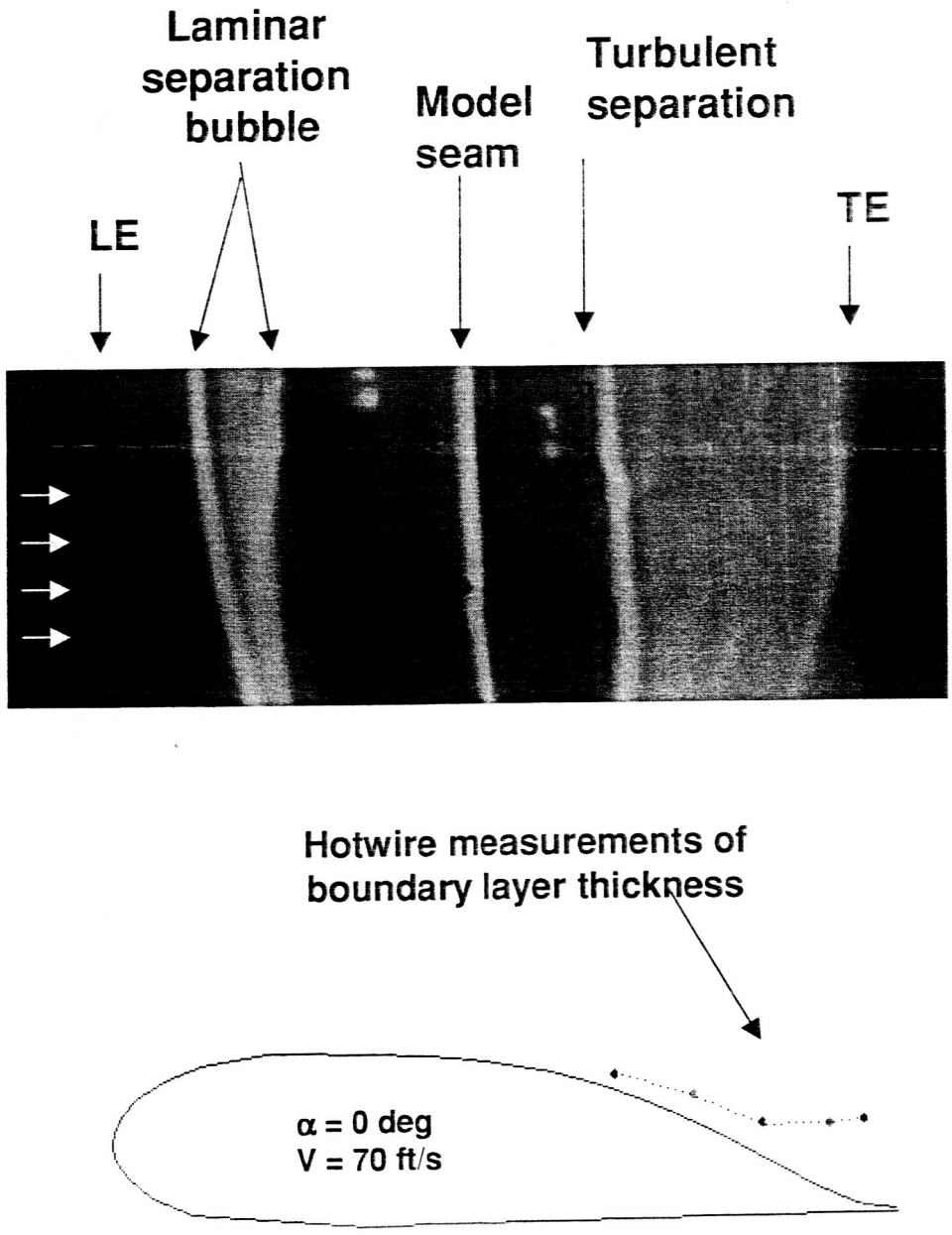

Fig. 15 Surface flow visualization and boundary layer measurements at $\alpha = 0°$, $r_{LE}/c = 0.05$, $\Delta r_t/R = 0.01$, $V_o = 41\ kts$, $9000\ RPM$.

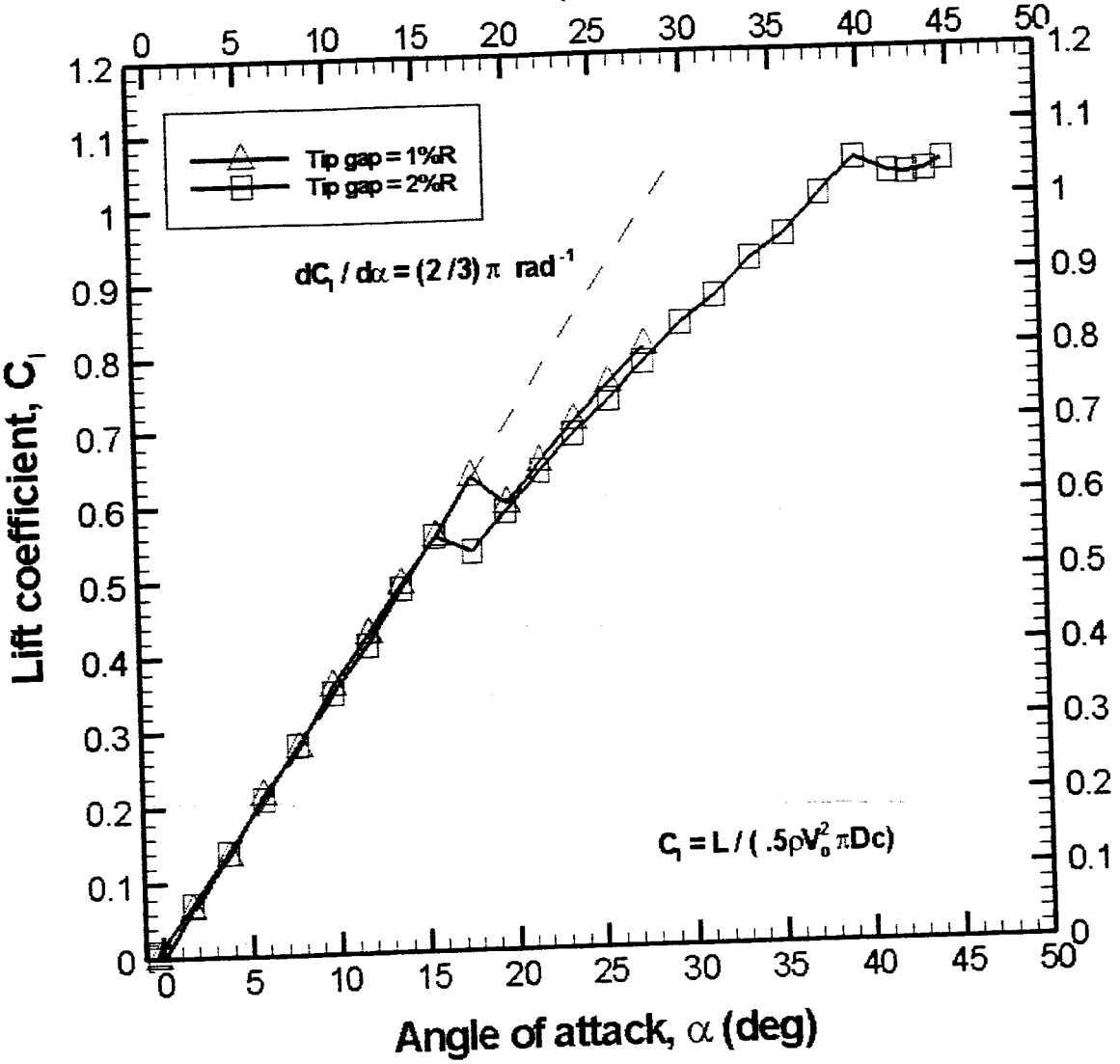

Fig. 16 Effect of tip gap on stall performance, $r_{LE}/c = 0.05$, $V_o = 35$ *kts*, 9000 *RPM*.

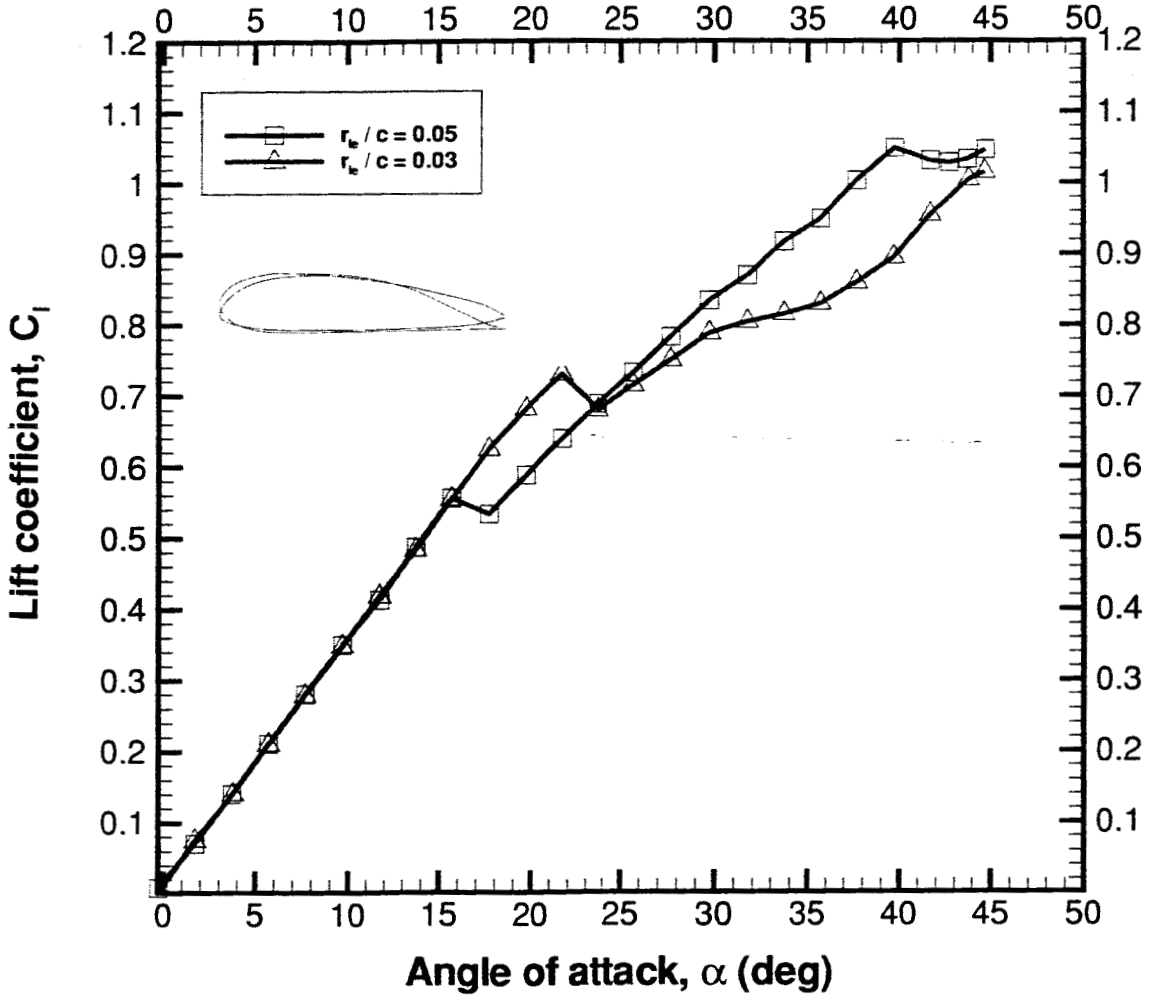

Fig. 17 **Effect of duct leading edge radius on stall performance: lift coefficient,** $\Delta r_l/R = 0.02$, $V_o = 35$ *kts*, 9000 *RPM*.

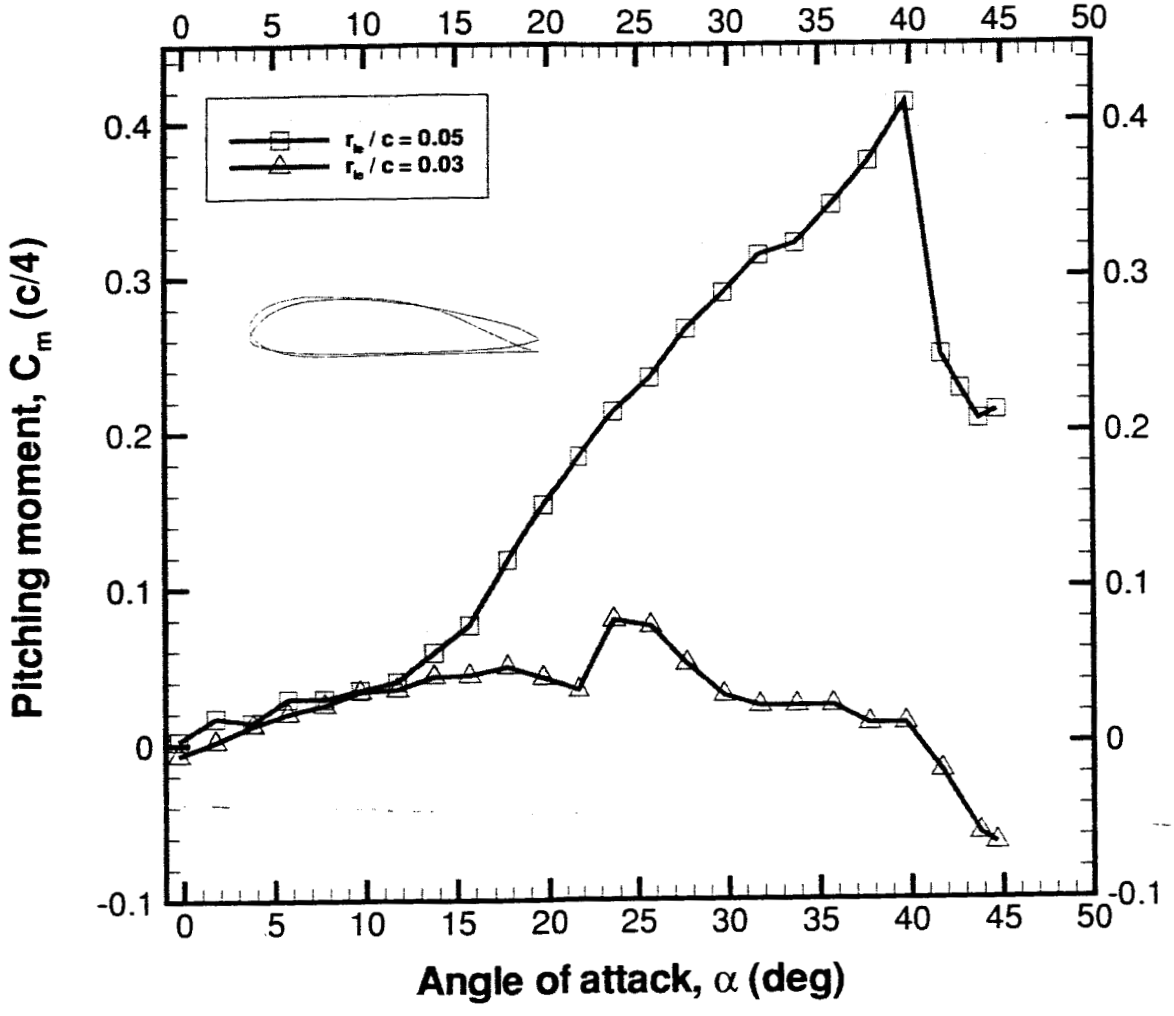

Fig. 18 Effect of duct leading edge radius on stall performance: pitching moment. $\Delta r_t/R = 0.02$, $V_o = 35\ kts$, $9000 RPM$.

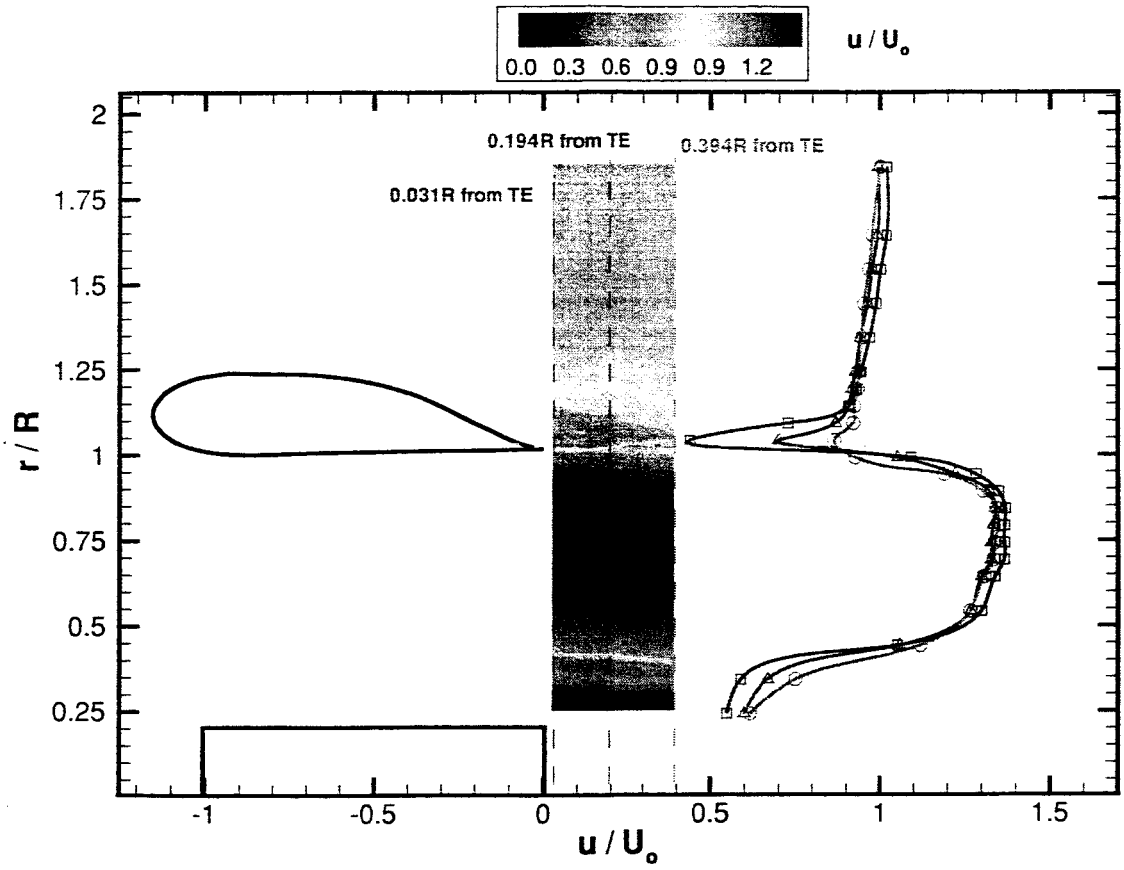

Fig. 19 Duct exit velocity profiles in propeller mode at $\alpha = 0°$, $r_{LE}/c = 0.05$, $\Delta r_t/R = 0.01$, $V_o = 41\ kts$, $9000RPM$.

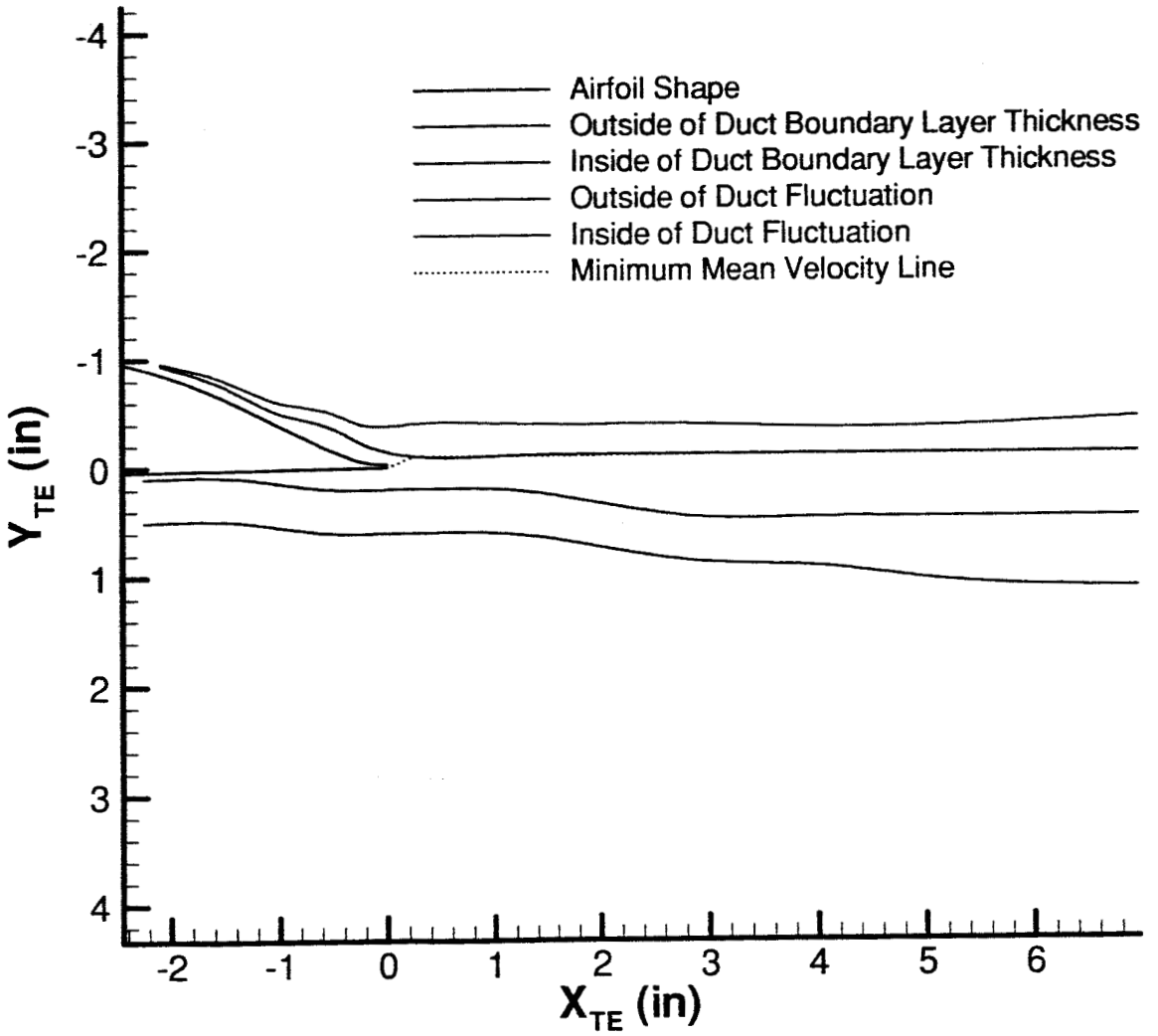

Fig. 20 Measured internal/external boundary layer geometry and duct exit wake thickness in propeller mode at $\alpha = 0°$, $r_{LE}/c = 0.05$, $\Delta r_t/R = 0.01$, $V_o = 41$ *kts*, 9000*RPM*.

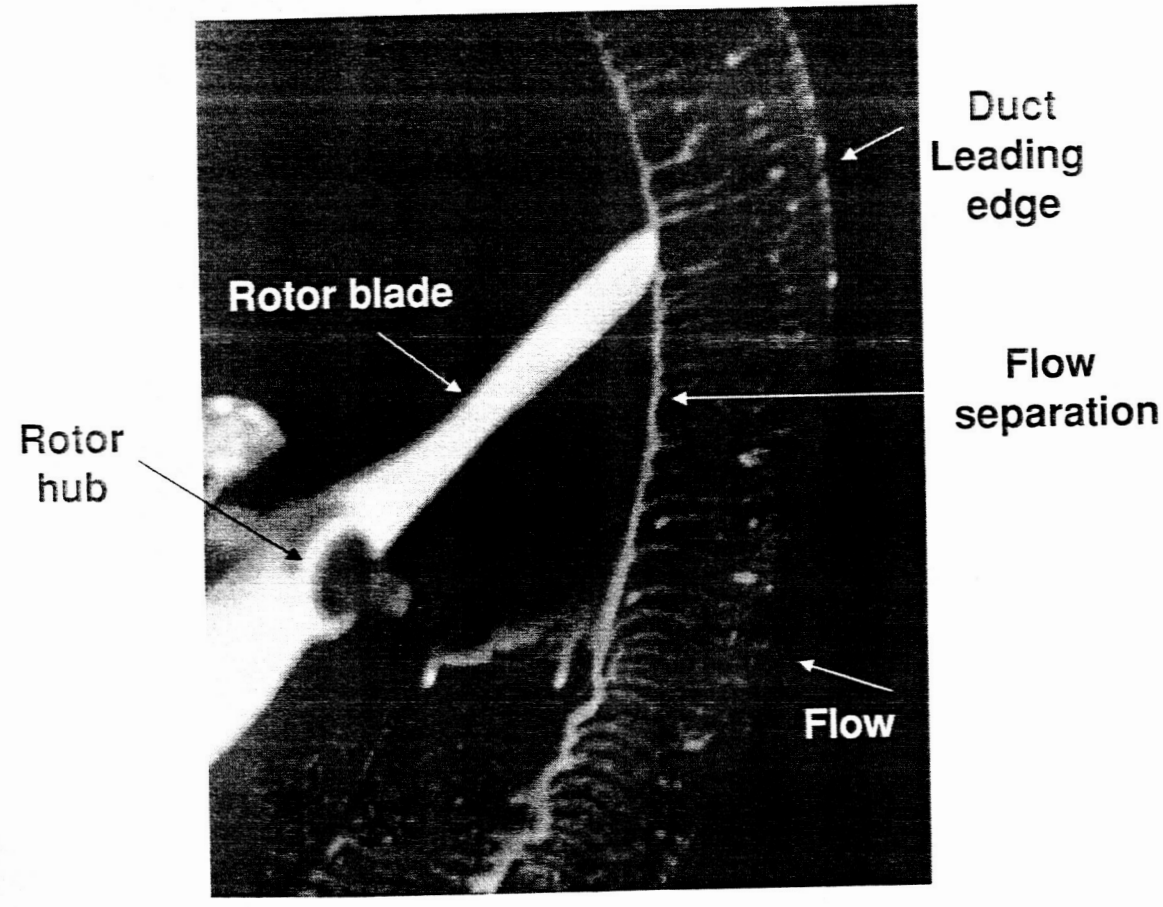

Fig. 21 Surface flow visualization of rotor induced separation in tip path plane, propeller mode at $\alpha = 0°$, $r_{LE}/c = 0.05$, $\Delta r_t/R = 0.02$, $V_0 = 41\ kts$, $9000RPM$.